The Astrophysical Journal, 932:13 (8pp), 2022 June 10 https://doi.org/10.3847/1538-4357/ac6c83

Interpreting the Statistical Properties of High-z Extragalactic Sources Detected by the South Pole Telescope Survey

Zhen-Yi Cai[1,2], Mattia Negrello[3], and Gianfranco De Zotti[4]
[1] CAS Key Laboratory for Research in Galaxies and Cosmology, Department of Astronomy, University of Science and Technology of China, Hefei 230026, People's Republic of China; zcai@ustc.edu.cn
[2] School of Astronomy and Space Science, University of Science and Technology of China, Hefei 230026, People's Republic of China
[3] School of Physics and Astronomy, Cardiff University, The Parade, Cardiff CF24 3AA, UK; NegrelloM@cardiff.ac.uk
[4] INAF, Osservatorio Astronomico di Padova, Vicolo dell'Osservatorio 5, I-35122 Padova, Italy; gianfranco.dezotti@inaf.it
Received 2022 April 1; revised 2022 April 26; accepted 2022 May 2; published 2022 June 9

Abstract

The results of the recently published spectroscopically complete survey of dusty star-forming galaxies detected by the South Pole Telescope over 2500 deg^2 proved to be challenging for galaxy formation models that generally underpredict the observed abundance of high-z galaxies. In this paper we interpret these results in the light of a physically grounded model for the evolution of spheroidal galaxies. The model accurately reproduces the measured redshift distribution of galaxies without any adjustment of the parameters. The data do not support the indications of an excess of $z > 4$ dusty galaxies reported by some analyses of Herschel surveys.

Unified Astronomy Thesaurus concepts: High-redshift galaxies (734)

1. Introduction

Ever since the far-IR to millimeter region opened up to astrophysical investigations it has been a game changer. The InfraRed Astronomy Satellite (IRAS; Neugebauer et al. 1984) revealed that in the local universe a substantial fraction ($\simeq$30%) of starlight is absorbed and reprocessed by dust, implying that far-IR observations are a key player in extragalactic astrophysics. This became even clearer with Cosmic Background Explorer (COBE) measurements of the cosmic infrared background (CIB) absolute energy spectrum (Puget et al. 1996; Fixsen et al. 1998), which was found to have approximately the same brightness as the optical background (Dole et al. 2006), implying that a large fraction of starlight was reprocessed by dust and that the reprocessed fraction was higher at high redshifts, as quantitatively predicted by Franceschini et al. (1991).

The 850 μm surveys with the Submillimeter Common-User Bolometer Array (SCUBA) on the James Clerk Maxwell Telescope (JCMT; e.g., Smail et al. 1997; Hughes et al. 1998; Barger et al. 1998) demonstrated not only that the most active star formation phases of high-z galaxies are heavily dust-enshrouded and therefore largely missed by optical/UV surveys, but also that the abundance of ultraluminous high-z galaxies is much larger than predicted by the leading merger-driven galaxy formation models of the time (e.g., Kaviani et al. 2003; Baugh et al. 2005) and more consistent with self-regulated galaxy–active galactic nucleus (AGN) coevolution (Granato et al. 2001, 2004; Lapi et al. 2006, 2011, 2014; Cai et al. 2013).

A new challenge came from searches for submillimeter selected $z \gtrsim 4$ galaxies using Herschel Spectral and Photometric Imaging Receiver (SPIRE) survey data (Dowell et al. 2014; Asboth et al. 2016; Ivison et al. 2016); the derived abundances are well above model predictions. The issue is still debated however. Béthermin et al. (2017) argued that due to its limited angular resolution, the SPIRE photometry may be affected by flux boosting due to instrumental noise and confusion (including the contribution from clustering). Some studies (Donevski et al. 2018; Duivenvoorden et al. 2018) suggested that indeed the discrepancy with models might be accounted for by these effects.

On the other hand, Cai et al. (2020) showed that an excess of high-z galaxies over model predictions had to be expected in the presence of the top-heavy stellar initial mass function (IMF) inferred by Zhang et al. (2018) to account for the low $^{13}C/^{18}O$ abundance ratio found in four gravitationally lensed submillimeter galaxies at $z \sim 2$–3. A top-heavy IMF was advocated also by Katz et al. (2022) to account for the [O III]88 μm–star formation rate (SFR) and [C II]158 μm–SFR relations observed at $z > 6$.

However, firm conclusions on space densities of high-z galaxies were hampered by the uncertainties on source redshifts, which were mostly photometric. The sample of 81 galaxies with full spectroscopic completeness and proper deboosting (Reuter et al. 2020), drawn from the South Pole Telescope Sunyaev–Zeldovich (SPT–SZ) survey covering $\simeq$2530 deg^2 (Everett et al. 2020), is allowing us to put the analysis on more solid grounds. The theoretical framework is presented in Section 2, the completeness of the Reuter et al. (2020) is discussed in Section 3, and in Section 4 the observed redshift distribution is compared to model predictions for different IMFs. The main conclusions are summarized in Section 5.

We adopt a flat ΛCDM cosmology with parameters derived from Planck cosmic microwave background power spectra: $H_0 = 67.4$ km s^{-1} Mpc^{-1} and $\Omega_m = 0.315$ (Planck Collaboration VI 2020).

2. Theoretical Framework

The ages of stellar populations in galaxies demonstrate (see Figure 10 of Bernardi et al. 2010) that at $z \gtrsim 1.5$, i.e., in the redshift range of interest here, most of the star formation activity is associated with massive protospheroidal galaxies, consistent with the downsizing scenario (e.g., Thomas et al. 2010). Evidence of a morphological transition of dusty galaxies

at $z \sim 1.25$ was reported by Ling & Yan (2022), based on Hubble Space Telescope (HST) images of samples from the Herschel Multi-tiered Extragalactic Survey (HerMES; Oliver et al. 2012) and from SCUBA2 surveys of the Cosmic Evolution Survey (COSMOS; Scoville et al. 2007) field, covering the redshift range $0.5 < z < 3$. At lower redshifts such galaxies are predominantly disk galaxies; at higher redshifts they are predominantly irregular/interacting systems that are expected to evolve into spheroidal galaxies. Indications of morphological evolution, occurring at $z \sim 1.4$, were pointed out by Zavala et al. (2018). These authors argued that data on galaxies detected by their very deep SCUBA2 survey, imaged with HST, can be interpreted in terms of an evolutionary path whereby galaxies classified by them as "irregular disks" are the precursors of present-day ellipticals.

A physically grounded model for the formation and evolution of these objects was provided by Cai et al. (2013). The model adopts as the halo formation rate, a function of halo mass and redshift, the positive term of the time derivative of the halo mass function. Such a derivative was computed using the analytical approximation by Sheth & Tormen (1999). The star formation and the growth of the active nucleus (the AGN) are triggered by the first, fast collapse phase of the halo, including major mergers, as highlighted by high-resolution *N*-body simulations (e.g., Wang et al. 2011). The subsequent slow growth of the halo outskirts by minor mergers and diffuse accretion has little effect on the inner part of the potential well, where the visible galaxy resides. Star formation and nuclear activity are governed by in situ processes described by a set of equations including gas cooling, condensation into stars, radiation drag, accretion onto the central supermassive black hole, and feedback from supernovae and from the active nucleus. Numerically solving these equations we obtain SFRs and accretion rates as a function of halo mass, formation redshift, and galactic age.

SFRs are converted into total infrared (IR; 8–1000 μm) luminosities, $L_{\rm IR}$, using the standard calibration (e.g., Kennicutt & Evans 2012). The bolometric luminosity functions of galaxies, of AGNs, and of objects as a whole (galaxy plus AGN) at each z are obtained coupling the luminosity as a function of halo mass with the halo formation rate. Monochromatic luminosity functions of galaxies are derived adopting appropriate spectral energy distributions. The effect of gravitational lensing on observed counts and luminosity functions is also taken into account.

This approach was the only one which successfully predicted the SPT and the Herschel Spectral and Photometric Imaging Receiver (SPIRE) counts of strongly lensed galaxies (Vieira et al. 2010; Negrello et al. 2010). The Cai et al. (2013) model accurately reproduced a broad variety of multifrequency data (source counts, redshift distributions, multiepoch luminosity functions) as reported in the paper itself, as well as later data (Cai et al. 2014; Carniani et al. 2015; Bonato et al. 2014, 2017, 2019; De Zotti et al. 2019; Gralla et al. 2020); see also Figure 1.

Cai et al. (2020) addressed the issue of the abundance of $z > 4$ galaxies detected by Herschel/SPIRE surveys pointing out the important effect of the stellar IMF. The interpretation of the controversial excess of $z > 4$ dusty galaxies in terms of a top-heavy IMF was however inconclusive, largely due to uncertainties on photometric redshifts. The SPT sample with fully spectroscopic redshifts is thus an important advance. However, to properly compare the observed redshift distribution with model predictions we need to assess the completeness of the Reuter et al. (2020) sample.

3. Completeness of the Sample

The Reuter et al. (2020) contains 45 galaxies with deboosted flux density at 1.4 mm (220 GHz) $S_{1.4\ \rm mm,deb} \geqslant 20$ mJy. The adopted limit is a trade-off between sample size and completeness. The Reuter et al. (2020) sample was generated from a parent sample of 4.5σ detections above a raw flux density of approximately 20.4 mJy at 1.4 mm (Everett et al. 2020). As discussed below, the completeness of the Everett et al. (2020) sample above the chosen flux limit is $\simeq$50%.

One of the Reuter et al. (2020) sources (SPT2037-65) is not included in the parent catalog, probably because it lies at the edge of the survey field and was cut in the mask construction process (J. Vieira 2022, personal communication). According to the discussion in Reuter et al. (2020), none of the 45 galaxies shows indications of multiplicity, i.e., of being a protocluster candidate. Also, none of these sources is included in the sample of protocluster core candidates by Wang et al. (2021).

In the Everett et al. (2020) catalog there are nine additional "dust" type sources with $S_{1.4\ \rm mm,best} \geqslant 20$ mJy and a cut classification "2" (Table 1).[5] This flag identifies the "z cut" subsample that excludes all sources flagged as stars or with cross-matched redshifts $z \leqslant 0.1$ or with angular sizes $\gtrsim 1'$ (see Section 4.10 of Everett et al. 2020 for details). Therefore, these nine sources are expected to be high-z strongly lensed galaxies. One of them (J032538-5247.1), however, can be identified with the local galaxy IC 1933 and we dropped it.

We searched for the other eight sources in the Herschel/SPIRE point source catalog[6] using a search radius of 35″, the quadratic sum of the 3σ SPT (at 1.4 mm) and SPIRE astrometric uncertainties, 34″(see Section 3.7 of Everett et al. 2020)) and $\simeq 10''$ (Bourne et al. 2016), respectively. We have chosen the FLUX photometry that, according to the SPIRE Point Source Catalog Explanatory Supplement[7] "has proven to be superior to a number of other common methods used with SPIRE data in terms of reproducibility and photometric accuracy, down to fluxes of 30 mJy" (Pearson et al. 2014). We retrieved photometric data for four galaxies (see Table 1). A source was detected by SPIRE also in the field of J225737 −6116.0, but, as discussed below, it is most likely associated with a nearby radio source. In fact, the SPIRE flux densities (46.8 ± 3.6, 52.6 ± 3.3, and 46.5 ± 3.2 at 500, 350, and 250 μ m, respectively) do not match the SPT photometry.

Photometric redshifts were estimated by fitting the Herschel/SPIRE and the SPT photometry (except for that at 95 GHz, which may be contaminated by radio emission) with the spectral energy distribution (SED) of high-z protospheroidal galaxies by Cai et al. (2013, see their Figure 2). The best-fit photo-z and their 68% confidence errors were computed using the routine MPFIT,[8] which performs a χ^2 minimization. The results are reported in Table 1.

In the Everett et al. (2020) catalog, a $z = 0.2627$ is ascribed to J000613-5620.7, which is 5.″6 apart from the SPT position.

[5] Reuter et al. (2020) and Everett et al. (2020) use a slightly different notation for deboosted flux densities, denoted as $S_{\rm deb}$ and $S_{\rm best}$, respectively.

[6] http://archives.esac.esa.int/hsa/whsa/

[7] archives.esac.esa.int/hsa/legacy/HPDP/SPIRE/SPIRE-P/SPSC/SPIREPointSourceCatalogExplanatorySupplementFull20170203.pdf

[8] https://pages.physics.wisc.edu/~craigm/idl/fitting.html

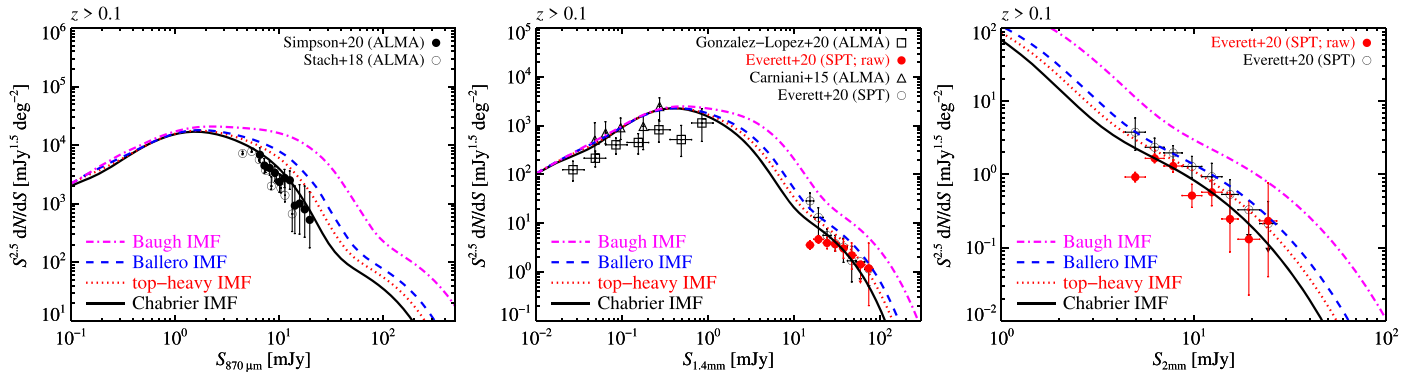

Figure 1. Euclidean normalized differential counts at 870 μm, 1.4 mm, and 2 mm: predictions of the Cai et al. (2013) model (solid black lines) compared with observational estimates by Stach et al. (2018) and Simpson et al. (2020) at 870 μm, and of Everett et al. (2020) at 1.4 and 2 mm. The latter counts are the "z cut" ones, i.e., those obtained removing galaxies at $z \leqslant 0.1$; obviously such galaxies are removed also from model predictions. The filled red circles show our own counts at 1.4 and 2 mm derived from the Everett et al. (2020) catalog, not corrected for incompleteness (see the text). At 1.4 mm we have added the deep counts by Carniani et al. (2015) at 1.3 mm and by González-López et al. (2020) at 1.24 mm. The flux densities at the latter wavelengths have been scaled to 1.4 mm using the protospheroidal SED by Cai et al. (2013). The scaling factors are very weakly dependent on redshift for $z < 8$; their mean values are 0.80 and 0.65, respectively. The dotted, dashed, and dotted–dashed lines refer to top-heavier IMFs specified in the inset (see Section 4).

This redshift was measured for a radio galaxy, WISEA J000613.47-562042.4. However, the 250 μm/1.4 mm flux density ratio of J000613-5620.7 is indicative of a much higher redshift. The $z = 0.2627$ may belong to the galaxy acting as the lens. The top-left panel of Figure 2 shows the SPT plus SPIRE photometry together with the data on the radio galaxy reported in the NASA/IPAC Extragalactic Database (NED). The global SED can be interpreted as the sum of a background dusty galaxy at $z \simeq 4.2$ with the radio galaxy. The synchrotron component of the latter has a blazar SED, which, in the considered frequency range, can be represented as (Massardi et al. 2022)

$$S_\nu = A \Big/ \left[\left(\frac{\nu}{\nu_0} \right)^\alpha + \left(\frac{\nu}{\nu_0} \right)^\beta \right], \qquad (1)$$

with $\alpha \lesssim 0.5$ and $\beta > 1$. The fit shown has $\alpha = 0.15$, $\beta = 1.20$, and $\log(\nu_0/\mathrm{Hz}) \simeq 12.9$. Note that, here and in the following, we do not include in the fit the sub-GHz (SUMSS or RACS) flux densities because they are frequently affected by self-absorption or by excesses due to other components. The blazar dominates the 95 GHz flux density and contributes substantially also at 150 GHz. The near-infrared (NIR)–optical excess is interpreted as due to the blazar host galaxy whose SED is modeled using the Ell2 template taken from the SWIRE library[9] (Polletta et al. 2007) with a bolometric luminosity $\log(L_{\rm bol}/L_\odot) \simeq 11.0$. The submillimeter peak is fitted by the protospheroidal template of Cai et al. (2013) at $z \simeq 4.2$; the IR (8–1000 μm) luminosity is $\log(\mu L_{\rm IR}/L_\odot) \simeq 13.7$, μ being the gravitational magnification.

The source J015539−5829.1 may be identified with the radio source PMN J0155−5829 (separation of 10.″7), with a flux density of 44 ± 8 mJy at 4.85 GHz, and with the galaxy WISEA J015539.00-582859.9 (separation of 10″). The global SED has a blazar shape (Equation (1)) with $\alpha \simeq 0.38$, $\beta = 1.20$, and $\log(\nu_0/\mathrm{Hz}) \simeq 13.3$; therefore, we have removed it from our sample. The NIR–optical excess, likely due to the host galaxy, is fitted by a SWIRE Ell2 template at $z \simeq 0.44$ with a bolometric luminosity $\log(L_{\rm bol}/L_\odot) \simeq 11.7$ (see the top-middle panel of Figure 2).

[9] http://www.iasf-milano.inaf.it/~polletta/templates/swire_templates.html

J032837-6447.4 is ≃10″ away from the galaxy WISEA J032839.00-644728.6. If this galaxy can be identified with the SPT source, a fit using the SWIRE Spi4 SED yields a photometric redshift $z \simeq 1.0$ (see the top-right panel of Figure 2) and $\log(L_{\rm IR}/L_\odot) \simeq 12.7$, qualifying it as an ultraluminous IR galaxy (ULIRG).

As for J051445−6449.1, the SPIRE catalog contains a 500 μm detection at 25.″3 from the SPT position. There is also a 350 μm detection but 31″ away from the one at 500 μm. This suggests that J051445−6449.1 is extended with emissions at the two wavelengths peaking at different positions. In fact, this source may be identified with a Planck Galactic Cold Clump (PGCC; Planck Collaboration et al. 2016), although we caution that several PGCCs turned out to be high-z strongly lensed galaxies (Trombetti et al. 2021). The extendness hypothesis is confirmed by the lack of detection by Large Apex Bolometer Camera (LABOCA) observations at 870 μm with an angular resolution (FWHM) of 19.″7 and median rms sensitivity of 8 mJy (Greve et al. 2012; J. Vieira 2022, private communication). Therefore, this source was not considered further.

J201445−4152.0 was detected in all three SPIRE bands (nominal separations from the SPT position in the range 10.″2–11.″7, depending on the SPIRE band). The SPT and SPIRE data are reasonably well fitted by the Cai et al. (2013) protospheroidal SED at $z \simeq 3.6$, with $\log(\mu L_{\rm IR}/L_\odot) \simeq 13.7$. It is 11.″5 away from WISEA J201446.90-415207.3, which may be the lens. Its SED is fitted by the SWIRE TQSO1 template at $z \simeq 0.5$ with $\log(L_{\rm bol}/L_\odot) \simeq 11.2$ (see the bottom-left panel of Figure 2).

For J213230-4537.8 we found a SPIRE detection at 250 μm (separation of 21″). Our fit of the SPT photometry at >95 GHz and of the SPIRE photometry yielded $z \simeq 3.9$ and $\log(\mu L_{\rm IR}/L_\odot) \simeq 13.7$; the fitting SED is fully consistent with the WISE flux densities of WISEA J213231.44-453749.0 (separation of 13″ from the nominal SPT position), which is the likely identification (see the bottom-middle panel of Figure 2). This galaxy is 37.″2 away from WISEA J213228.32-453738.2, which may be identified with the blazar AT20G J213227-453740 (the separation among the nominal positions of the two objects is 2.″9). Thus, the blazar lies within the FWHM of the 95 GHz beam (FWHM = 1.″7) and can therefore account for the flux density excess at this frequency (it has a flux density of

Table 1
SPT Sources in the Everett et al. (2020) "z cut" Subsample with $S_{220\ \mathrm{GHz,deb}} \geqslant 20$ mJy Not in the Reuter et al. (2020) Sample

SPT ID	R.A.	Decl.	$S_{95\ \mathrm{GHz,deb}}$	$S_{150\ \mathrm{GHz,deb}}$	$S_{220\ \mathrm{GHz,deb}}$	$S_{500\ \mu\mathrm{m}}$	$S_{350\ \mu\mathrm{m}}$	$S_{250\ \mu\mathrm{m}}$	Redshift	Note
J000613-5620.7*	1.55824	−56.34621	$13.2^{+2.1}_{-2.3}$	$14.5^{+1.4}_{-1.2}$	30.4 ± 3.0			47.6 ± 4.3	0.2627	$z_{\mathrm{phot}} \simeq 4.2 \pm 0.2$
J015539-5829.1	28.91375	−58.48602	19.7 ± 2.2	$11.5^{+1.4}_{-1.3}$	20.2 ± 4.1				none	Radio source
J032538-5247.1	51.41249	−52.78567	$2.1^{+1.7}_{-1.0}$	5.9 ± 1.2	$20.9^{+4.1}_{-4.3}$				none	IC 1933
J032837-6447.4*	52.15700	−64.79109	$1.0^{+0.7}_{-0.3}$	$5.7^{+1.0}_{-0.9}$	21.8 ± 3.5				none	$z_{\mathrm{phot}} \simeq 1.0 \pm 0.002$
J051445-6449.1	78.69093	−64.81905	$1.5^{+1.4}_{-0.6}$	$6.5^{+1.4}_{-1.0}$	24.5 ± 4.9	98.9 ± 5.7	72.6 ± 3.8	—	none	PGCC
J201445-4152.0*	303.69122	−41.86763	$2.2^{+1.9}_{-1.1}$	7.2 ± 1.4	$22.2^{+5.0}_{-5.1}$	115.6 ± 5.0	117.8 ± 4.1	69.3 ± 3.5	none	$z_{\mathrm{phot}} \simeq 3.6 \pm 0.1$
J213230-4537.8*	323.12610	−45.63134	7.3 ± 2.5	$5.0^{+1.2}_{-1.0}$	$22.4^{+4.7}_{-5.3}$			51.9 ± 5.4	1.332	$z_{\mathrm{phot}} \simeq 3.9 \pm 0.2$
J225737-6116.0	344.40634	−61.26759	7.8 ± 2.3	6.6 ± 1.3	$24.1^{+4.8}_{-5.0}$				none	Radio source, cirrus
J232216-4836.2	350.56729	−48.60440	$11.5^{+2.3}_{-2.1}$	$7.7^{+1.4}_{-1.2}$	22.3 ± 4.9				none	Radio source

Note. Note that S_{deb} is called S_{best} by Everett et al. (2020). Flux densities are in mJy. Photometric redshifts listed in the last column were obtained as described in the text. The errors on z_{phot} are those yielded by the fitting routine. The real uncertainties are much larger and associated with the choice of the SED used for the fit. The four sources in boldface marked with asterisks are probably high-z dusty galaxies (see Section 3).

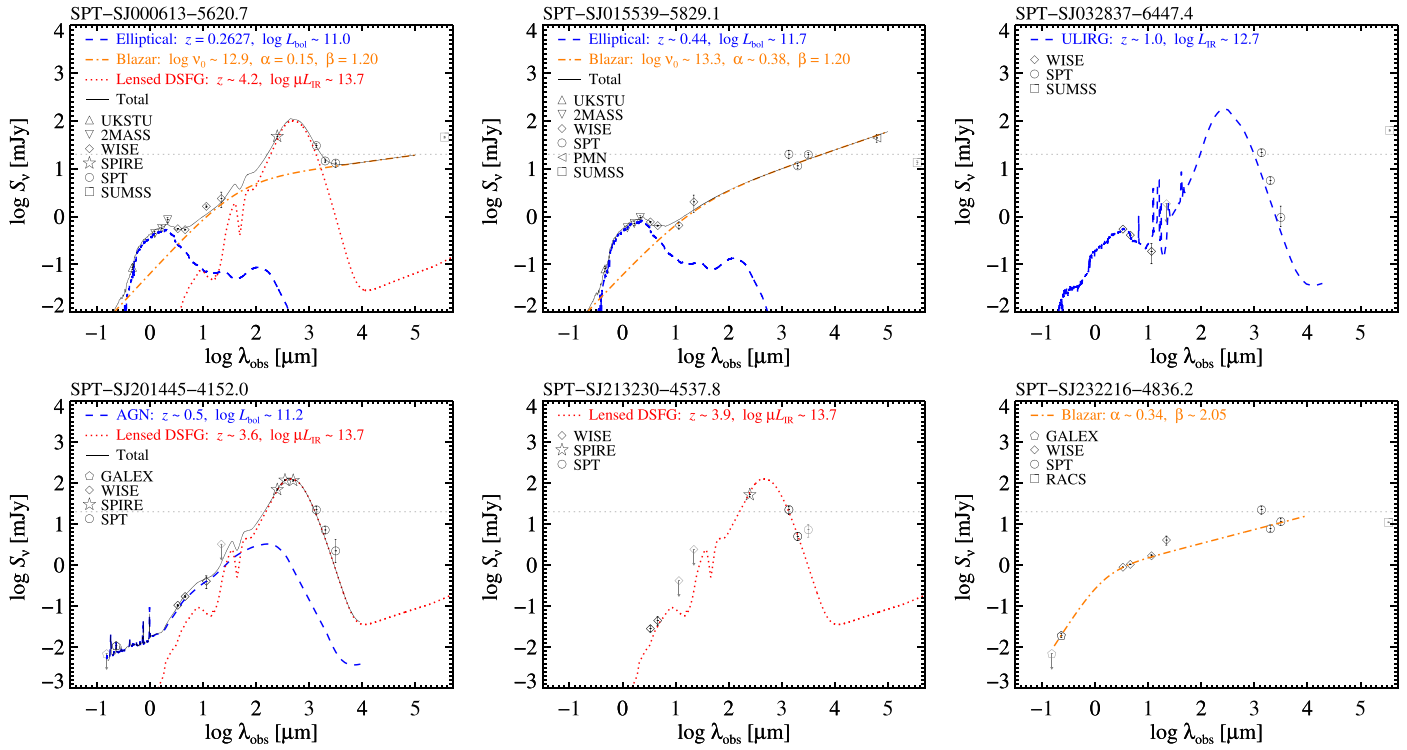

Figure 2. Fits of multiwavelength data for the six sources in Table 1 discussed in the text. Extra data on likely counterparts are from the Galaxy Evolution Explorer (GALEX; Martin et al. 2005), the United Kingdom Schmidt Telescope Unit (UKSTU; Maddox et al. 1990), the Two Micron All Sky Survey (2MASS; Skrutskie et al. 2006), the Wide-field Infrared Survey Explorer (WISE; Wright et al. 2010), the Parkes-MIT-NRAO (PMN) survey (Wright et al. 1994), the Sydney University Molonglo Sky Survey (SUMSS; Mauch et al. 2003), and the Rapid ASKAP Continuum Survey (RACS; Hale et al. 2021). A single SED or a combination of two/three SEDs, including the Cai et al. (2013) protospheroidal SED (red dotted line), a specific SWIRE SED (blue dashed line), and/or a typical blazar SED (orange dotted–dashed line), are used to fit the data in black (see the text).

73 ± 4 mJy at 20 GHz). Its continuum spectrum, however, must drop rapidly above 20 GHz (the SPT flux density at 95 GHz is 7.3 ± 2.5 mJy) and its observed flux density is substantially attenuated at the higher SPT frequencies because of the lower FWHM; it is thus likely that the blazar contribution at these frequencies is small.

J225737-6116.0 is 17.″9 away from the radio source SUMSS J225739-611606 which is well within the SPT beam at 95 GHz. The radio source has a flux density of 143.01 ± 1.88 mJy at 0.863 GHz and, if it is flat-spectrum, it may dominate at 95 GHz where the data show an excess over a dusty galaxy SED. Subtracting its contribution at 220 GHz, the flux density may drop below the adopted threshold of 20 mJy. There are detections at all three SPIRE wavelengths with separations of $\simeq 6''$ from the radio source (which is therefore the likely counterpart to the Herschel source) and at 20″–23″ from the SPT position. The SPT source lies in a cirrus region and was not detected with LABOCA at 870 μm (J. Vieira 2022, private communication), implying that it is not a dusty galaxy and will not be considered further.

J232216-4836.2 is 2.″2 away from the radio source RACS-DR1 J232215.9-483615 (McConnell et al. 2020; Hale et al. 2021) with a flux density of 11.0 ± 0.3 mJy beam^{-1} at 0.855 GHz. In turn, the RACS source is 1.″4 apart from WISEA J232215.92-483616.2. Identifying the three sources we get the SED shown in the bottom-right panel of Figure 2, indicating that this source is a blazar. It was therefore excluded from our sample.

In conclusion we decided to keep J000613-5620.7, J032837-6447.4, J201445-4152.0, and J213230-4537.8, while J015539-5829.1, J051445-6449.1, J225737-6116.0, and J232216-4836.2 were dropped.

We have included the three additional likely strongly lensed sources with photometric redshift estimates in the redshift distribution for $S_{1.4\,\mathrm{mm,best}} \geqslant 20$ mJy (J032837−6447.4 is probably an unlensed ULIRG). This brings the completeness of the Reuter et al. (2020) sample at the level of the Everett et al. (2020) sample. The three sources have redshifts in the range 3.6–4.2 and fill the dip shown by the Reuter et al. (2020) sample.

The completeness of the latter is discussed by Everett et al. (2020). The area was divided into 19 contiguous fields, observed independently. The flux density corresponding to 95% completeness varies from field to field. At 220 GHz it ranges from 16.19 to 29.70 mJy with a median of 26.83 mJy. The completeness as a function of flux density, $f_{\mathrm{compl}}(S)$, was calculated by Everett et al. (2020) adding random locations to 100 simulated sources at fixed flux density values and applying their source extraction algorithm. The process was repeated at a few flux density levels spread over a broad range; $f_{\mathrm{compl}}(S)$ was computed as the ratio between the numbers of recovered and input sources. An error function was fitted to the results and adopted as a model for $f_{\mathrm{compl}}(S)$.

Since the model $f_{\mathrm{compl}}(S)$ is not given by Everett et al. (2020), we have estimated it by comparing the counts of dusty galaxies in the "z cut" subsample derived directly from the catalog with those, corrected for incompleteness, reported by Everett et al. (2020). The uncorrected counts at 220 GHz (1.4 mm) and 150 GHz (2 mm) are shown by the filled red circles in the central and right panels of Figure 1, respectively; the counts of "z cut" sources by Everett et al. (2020) for the same flux density bins are shown by the open circles. Our estimates of $f_{\mathrm{compl}}(S)$ at 1.4 mm are shown in Figure 3 (open

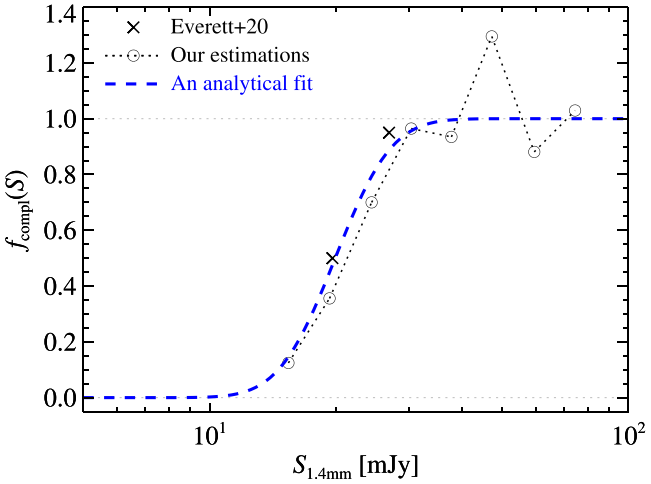

Figure 3. Completeness of the "z cut" sample at 1.4 mm (220 GHz) as a function of flux density, computed as described in the text. The open circles connected by the dotted line show the estimates for each flux density bin. The blue dashed line is the best-fit function, $f_{\rm compl}(S)$ (Equation (2)). The crosses correspond to the median flux densities at the 50% and 95% completeness levels across all fields, according to Table 3 of Everett et al. (2020), 19.65 and 26.83 mJy, respectively.

circles connected by the dotted broken line). The best-fit model in terms of the error function, represented by the dashed blue line, writes

$$f_{\rm compl}(S) = 0.5 \times \{1 + {\rm erf}[(\log S - 1.3)/0.15]\}. \quad (2)$$

The redshift distribution of sources with $S_{1.4\ {\rm mm,best}} \geqslant 20$ mJy was then computed assigning to each source, including those with just a photometric redshift estimate, the weight $1/f_{\rm compl}(S)$ corresponding to its flux density.

4. Model versus Data

In Figure 4, the redshift distribution of sources with $S_{1.4\ {\rm mm,best}} \geqslant 20$ mJy, tabulated in Table 2, is compared with predictions by Cai et al. (2020) for different choices of the IMF. The predictions of the phenomenological model by Béthermin et al. (2015, lensed galaxies only), extracted from Figure 10 of Reuter et al. (2020), are also shown for comparison. Béthermin et al. (2015) reported the redshift distribution of lensed galaxies with $S_{1.4\ {\rm mm}} > 20$ mJy yielded by the phenomenological model by Béthermin et al. (2012). As illustrated by Figure 4 the agreement with the data is reasonably good, although, as pointed out by Reuter et al. (2020), the predicted distribution peaks at a redshift somewhat lower than is observed.

Reuter et al. (2020) also compare their results with models by Hayward et al. (2013), Lagos et al. (2019), and Lovell et al. (2021). However the comparisons are tricky because these models do not include strong lensing. Published predictions must be extrapolated in frequency and in flux density in a complicated way since the flux density ratios depend on redshift. So the extrapolations cannot be accurate.

Figure 4 shows that the baseline model by Cai et al. (2013), adopting an universal Chabrier IMF, reproduces quite well the observed redshift distribution that is, however, also consistent with the "top-heavy" IMF proposed by Zhang et al. (2018). The "Ballero" (Ballero et al. 2007) IMF somewhat overpredicts the redshift distribution while the Baugh et al. (2005) IMF yields far too many high-z galaxies, as already found by Cai et al. (2020). In terms of $dN/d\log m$, m being the stellar mass, the

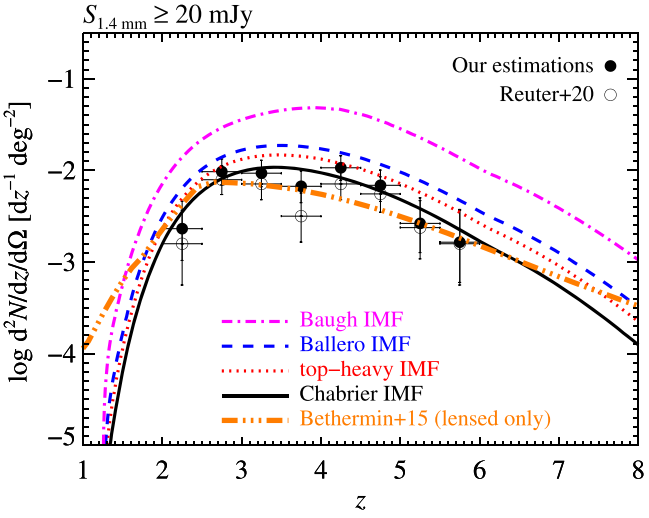

Figure 4. Redshift distribution of SPT–SZ sources brighter than $S_{220\ \rm GHz,deb} = 20$ mJy, corrected for incompleteness (filled black circles). The open circles show the redshift distribution of the 45 galaxies with $S_{220\ \rm GHz,deb} \geqslant 20$ mJy in the Reuter et al. (2020) sample, without any correction for incompleteness. The solid black line shows the prediction of the baseline model by Cai et al. (2013), adopting the Chabrier (2003) IMF. The other lines show the effect of adopting the top-heavier IMFs specified in the inset, following Cai et al. (2020). The redshift distribution predicted by the Béthermin et al. (2015) model is also plotted for comparison (dotted–dashed orange line).

Table 2
The Redshift Distribution of SPT Sources with $S_{1.4\ \rm mm,best} \geqslant 20$ mJy

z	$N_{\rm R20}$	$\frac{d^2N_{\rm R20}}{dzd\Omega}$ (10^{-3} dz^{-1} deg^{-2})	$N_{\rm our}$	$\frac{d^2N_{\rm our}}{dzd\Omega}$ (10^{-3} dz^{-1} deg^{-2})
(1)	(2)	(3)	(4)	(5)
2.25	$2^{+2.6}_{-1.3}$	$1.6^{+2.1}_{-1.0}$	$2.9^{+2.9}_{-1.6}$	$2.3^{+2.3}_{-1.3}$
2.75	$10^{+4.3}_{-3.1}$	$7.9^{+3.4}_{-2.5}$	$12.3^{+4.6}_{-3.5}$	$9.7^{+3.6}_{-2.7}$
3.25	$9^{+4.1}_{-2.9}$	$7.1^{+3.2}_{-2.3}$	$11.8^{+4.5}_{-3.4}$	$9.3^{+3.6}_{-2.7}$
3.75	$4^{+3.2}_{-1.9}$	$3.2^{+2.5}_{-1.5}$	$8.5^{+4.0}_{-2.9}$	$6.7^{+3.2}_{-2.3}$
4.25	$9^{+4.1}_{-2.9}$	$7.1^{+3.2}_{-2.3}$	$13.5^{+4.8}_{-3.6}$	$10.7^{+3.8}_{-2.9}$
4.75	$7^{+3.8}_{-2.6}$	$5.5^{+3.0}_{-2.0}$	$8.7^{+4.1}_{-2.9}$	$6.9^{+3.2}_{-2.3}$
5.25	$3^{+2.9}_{-1.6}$	$2.4^{+2.3}_{-1.3}$	$3.3^{+3.0}_{-1.7}$	$2.6^{+2.4}_{-1.4}$
5.75	$2^{+2.6}_{-1.3}$	$1.6^{+2.1}_{-1.0}$	$2.1^{+2.7}_{-1.3}$	$1.6^{+2.1}_{-1.0}$

Note. See also Figure 4. We adopted a bin size $\Delta z = 0.5$. The total area of the SPT survey is of 2530 deg^2. N_{R20} and $N_{\rm our}$ are the numbers of sources within each redshift bin from the Reuter et al. (2020) raw sample and from our updated sample corrected for incompleteness, respectively. The uncertainties are 1σ Poisson errors computed following Gehrels (1986).

"top-heavy" and the "Ballero" IMFs have power-law slopes above $0.5\,M_\odot$ of -1.1 and of -0.95, respectively; below $0.5\,M_\odot$ both have a slope of -0.3. The Chabrier (2003) IMF has a knee at $1\,M_\odot$ and power-law indices of -0.4 and -1.35 below and above that mass. The Baugh et al. (2005) IMF is $dN/d\log m = $ constant. Although our results are consistent with a universal Chabrier (2003) IMF, the degeneracies of the model leave room for improvements of the fits with the Zhang et al. (2018) IMF or even the Ballero et al. (2007) IMF, by adjusting the model parameters. On the other hand, we cannot get a reasonable fit with the Baugh et al. (2005) IMF.

We conclude that the Reuter et al. (2020) data tighten the constraints on the IMF at high z. However, a much larger sample is necessary to settle the issue on the "universality" of the Chabrier IMF. An important step forward will be possible

with the completion of the ongoing effort to obtain spectroscopic redshifts of bright ($S_{500\,\mu m} > 80$ mJy) Herschel-selected galaxies with photometric redshift $z_{phot} > 2$. The sample of such Herschel bright sources (HerBS), detected by the Herschel Astrophysical Terahertz Large Area Survey (H-ATLAS; Eales et al. 2010) covering an area of 616.4 deg^2, contains 209 galaxies (Bakx et al. 2018). Robust spectroscopic redshifts for 77% of the HerBS sample have already been acquired (Neri et al. 2020; Urquhart et al. 2022) using the NOrthern Extended Millimeter Array (NOEMA) and the Atacama Compact Array (ACA) facilities. The recently completed NOEMA large program z-Gal (PI: P. Cox) has yielded spectroscopic redshifts for 125 galaxies with $S_{500\,\mu m} > 80$ mJy also including galaxies in the Herschel Multi-tiered Extragalactic Survey (HerMES; Oliver et al. 2012) fields in the northern sky and in the equatorial region. The results are not public yet.

5. Conclusions

We have exploited the almost complete spectroscopic coverage of SPT galaxies with deboosted flux density at 1.4 mm $S_{1.4\,mm,deb} \geqslant 20$ mJy to investigate their redshift distribution, with particular attention to the controversial excess over model prediction of $z > 4$ galaxies. Such excess might indicate a top-heavier IMF in protospheroidal galaxies that dominate the star formation activity at high z (Cai et al. 2020). Observational evidence and theoretical arguments in these directions have indeed been put forward (Chiosi et al. 1998; Zhang et al. 2018; Romano et al. 2019; Katz et al. 2022), but the issue is still open and may have important implications for the understanding of galaxy evolution.

After applying careful corrections for incompleteness of the Reuter et al. (2020) sample and of the Everett et al. (2020) parent sample we found that the redshift distribution is accounted for quite well both by the physical model by Cai et al. (2013), adopting a universal Chabrier IMF, and by the phenomenological model by Béthermin et al. (2015), although the peak of the distribution predicted by the latter occurs at a redshift somewhat lower than is observed.

The data tighten the constraints on the high-z IMF, compared to the data discussed by Cai et al. (2020). While they are consistent with the moderately top-heavy IMF proposed by Zhang et al. (2018), they are in tension with the "Ballero" IMF that fitted the earlier data and are strongly inconsistent with the Baugh et al. (2005) IMF. The much larger sample that will be provided by the ongoing effort to obtain spectroscopic redshifts of bright ($S_{500\,\mu m} > 80$ mJy) Herschel-selected galaxies with photometric redshift $z_{phot} > 2$ will allow an important step forward toward settling the issue on the universality of the Chabrier IMF.

We are grateful to the referee for useful comments and to Joaquin Vieira for important information on SPT data. Z.Y.C. is supported by the National Science Foundation of China (grant Nos. 11873045, 11890693, and 12033006) and the USTC Research Funds of the Double First-Class Initiative (grant No. YD2030002009). This research has made use of the NASA/IPAC Extragalactic Database (NED) (2019), which is operated by the Jet Propulsion Laboratory, California Institute of Technology, under contract with the National Aeronautics and Space Administration. We also made use of the Herschel science archive (http://archives.esac.esa.int/hsa/whsa/), of data products from the Two Micron All Sky Survey (2MASS), from the Wide-field Infrared Survey Explorer (WISE) and from the Galaxy Evolution Explorer (GALEX). The 2MASS is a joint project of the University of Massachusetts and the Infrared Processing and Analysis Center/California Institute of Technology, funded by the National Aeronautics and Space Administration and the National Science Foundation. The WISE is a joint project of the University of California, Los Angeles, and the Jet Propulsion Laboratory/California Institute of Technology, funded by the National Aeronautics and Space Administration. The GALEX satellite was a NASA mission led by the California Institute of Technology.

ORCID iDs

Zhen-Yi Cai https://orcid.org/0000-0002-4223-2198
Mattia Negrello https://orcid.org/0000-0002-7925-7663
Gianfranco De Zotti https://orcid.org/0000-0003-2868-2595

References

Asboth, V., Conley, A., Sayers, J., et al. 2016, MNRAS, 462, 1989
Bakx, T. J. L. C., Eales, S. A., Negrello, M., et al. 2018, MNRAS, 473, 1751
Ballero, S. K., Kroupa, P., & Matteucci, F. 2007, A&A, 467, 117
Barger, A. J., Cowie, L. L., Sanders, D. B., et al. 1998, Natur, 394, 248
Baugh, C. M., Lacey, C. G., Frenk, C. S., et al. 2005, MNRAS, 356, 1191
Bernardi, M., Shankar, F., Hyde, J. B., et al. 2010, MNRAS, 404, 2087
Béthermin, M., Daddi, E., Magdis, G., et al. 2012, ApJL, 757, L23
Béthermin, M., De Breuck, C., Sargent, M., & Daddi, E. 2015, A&A, 576, L9
Béthermin, M., Wu, H.-Y., Lagache, G., et al. 2017, A&A, 607, A89
Bonato, M., De Zotti, G., Leisawitz, D., et al. 2019, PASA, 36, e017
Bonato, M., Negrello, M., Cai, Z. Y., et al. 2014, MNRAS, 438, 2547
Bonato, M., Negrello, M., Mancuso, C., et al. 2017, MNRAS, 469, 1912
Bourne, N., Dunne, L., Maddox, S. J., et al. 2016, MNRAS, 462, 1714
Cai, Z.-Y., De Zotti, G., & Bonato, M. 2020, ApJ, 891, 74
Cai, Z.-Y., Lapi, A., Bressan, A., et al. 2014, ApJ, 785, 65
Cai, Z.-Y., Lapi, A., Xia, J.-Q., et al. 2013, ApJ, 768, 21
Carniani, S., Maiolino, R., De Zotti, G., et al. 2015, A&A, 584, A78
Chabrier, G. 2003, PASP, 115, 763
Chiosi, C., Bressan, A., Portinari, L., & Tantalo, R. 1998, A&A, 339, 355
De Zotti, G., Bonato, M., Negrello, M., et al. 2019, FrASS, 6, 53
Dole, H., Lagache, G., Puget, J. L., et al. 2006, A&A, 451, 417
Donevski, D., Buat, V., Boone, F., et al. 2018, A&A, 614, A33
Dowell, C. D., Conley, A., Glenn, J., et al. 2014, ApJ, 780, 75
Duivenvoorden, S., Oliver, S., Scudder, J. M., et al. 2018, MNRAS, 477, 1099
Eales, S., Dunne, L., Clements, D., et al. 2010, PASP, 122, 499
Everett, W. B., Zhang, L., Crawford, T. M., et al. 2020, ApJ, 900, 55
Fixsen, D. J., Dwek, E., Mather, J. C., Bennett, C. L., & Shafer, R. A. 1998, ApJ, 508, 123
Franceschini, A., Toffolatti, L., Mazzei, P., Danese, L., & de Zotti, G. 1991, A&AS, 89, 285
Gehrels, N. 1986, ApJ, 303, 336
González-López, J., Novak, M., Decarli, R., et al. 2020, ApJ, 897, 91
Gralla, M. B., Marriage, T. A., Addison, G., et al. 2020, ApJ, 893, 104
Granato, G. L., De Zotti, G., Silva, L., Bressan, A., & Danese, L. 2004, ApJ, 600, 580
Granato, G. L., Silva, L., Monaco, P., et al. 2001, MNRAS, 324, 757
Greve, T. R., Vieira, J. D., Weiß, A., et al. 2012, ApJ, 756, 101
Hale, C. L., McConnell, D., Thomson, A. J. M., et al. 2021, PASA, 38, e058
Hayward, C. C., Narayanan, D., Kereš, D., et al. 2013, MNRAS, 428, 2529
Hughes, D. H., Serjeant, S., Dunlop, J., et al. 1998, Natur, 394, 241
Ivison, R. J., Lewis, A. J. R., Weiss, A., et al. 2016, ApJ, 832, 78
Katz, H., Rosdahl, J., Kimm, T., et al. 2022, MNRAS, 510, 5603
Kaviani, A., Haehnelt, M. G., & Kauffmann, G. 2003, MNRAS, 340, 739
Kennicutt, R. C., & Evans, N. J. 2012, ARA&A, 50, 531
Lagos, C. d. P., Robotham, A. S. G., Trayford, J. W., et al. 2019, MNRAS, 489, 4196
Lapi, A., González-Nuevo, J., Fan, L., et al. 2011, ApJ, 742, 24
Lapi, A., Raimundo, S., Aversa, R., et al. 2014, ApJ, 782, 69
Lapi, A., Shankar, F., Mao, J., et al. 2006, ApJ, 650, 42
Ling, C., & Yan, H. 2022, ApJ, 929, 40
Lovell, C. C., Geach, J. E., Davé, R., Narayanan, D., & Li, Q. 2021, MNRAS, 502, 772

Maddox, S. J., Sutherland, W. J., Efstathiou, G., & Loveday, J. 1990, MNRAS, 243, 692
Martin, D. C., Fanson, J., Schiminovich, D., et al. 2005, ApJL, 619, L1
Massardi, M., Bonato, M., Lopez-Caniego, M., et al. 2022, MNRAS, 513, 6013
Mauch, T., Murphy, T., Buttery, H. J., et al. 2003, MNRAS, 342, 1117
McConnell, D., Hale, C. L., Lenc, E., et al. 2020, PASA, 37, e048
NASA/IPAC Extragalactic Database (NED) 2019, NASA/IPAC Extragalactic Database (NED), IPAC, doi:10.26132/NED1
Negrello, M., Hopwood, R., De Zotti, G., et al. 2010, Sci, 330, 800
Neri, R., Cox, P., Omont, A., et al. 2020, A&A, 635, A7
Neugebauer, G., Habing, H. J., van Duinen, R., et al. 1984, ApJL, 278, L1
Oliver, S. J., Bock, J., Altieri, B., et al. 2012, MNRAS, 424, 1614
Pearson, C., Lim, T., North, C., et al. 2014, ExA, 37, 175
Planck Collaboration, Ade, P. A. R., Aghanim, N., et al. 2016, A&A, 594, A28
Planck Collaboration VI 2020, A&A, 641, A6
Polletta, M., Tajer, M., Maraschi, L., et al. 2007, ApJ, 663, 81
Puget, J. L., Abergel, A., Bernard, J. P., et al. 1996, A&A, 308, L5
Reuter, C., Vieira, J. D., Spilker, J. S., et al. 2020, ApJ, 902, 78
Romano, D., Matteucci, F., Zhang, Z.-Y., Ivison, R. J., & Ventura, P. 2019, MNRAS, 490, 2838
Scoville, N., Aussel, H., Brusa, M., et al. 2007, ApJS, 172, 1
Sheth, R. K., & Tormen, G. 1999, MNRAS, 308, 119
Simpson, J. M., Smail, I., Dudzevičiūtė, U., et al. 2020, MNRAS, 495, 3409
Skrutskie, M. F., Cutri, R. M., Stiening, R., et al. 2006, AJ, 131, 1163
Smail, I., Ivison, R. J., & Blain, A. W. 1997, ApJL, 490, L5
Stach, S. M., Smail, I., Swinbank, A. M., et al. 2018, ApJ, 860, 161
Thomas, D., Maraston, C., Schawinski, K., Sarzi, M., & Silk, J. 2010, MNRAS, 404, 1775
Trombetti, T., Burigana, C., Bonato, M., et al. 2021, A&A, 653, A151
Urquhart, S. A., Bendo, G. J., Serjeant, S., et al. 2022, MNRAS, 511, 3017
Vieira, J. D., Crawford, T. M., Switzer, E. R., et al. 2010, ApJ, 719, 763
Wang, G. C. P., Hill, R., Chapman, S. C., et al. 2021, MNRAS, 508, 3754
Wang, J., Navarro, J. F., Frenk, C. S., et al. 2011, MNRAS, 413, 1373
Wright, A. E., Griffith, M. R., Burke, B. F., & Ekers, R. D. 1994, ApJS, 91, 111
Wright, E. L., Eisenhardt, P. R. M., Mainzer, A. K., et al. 2010, AJ, 140, 1868
Zavala, J. A., Aretxaga, I., Dunlop, J. S., et al. 2018, MNRAS, 475, 5585
Zhang, Z.-Y., Romano, D., Ivison, R. J., Papadopoulos, P. P., & Matteucci, F. 2018, Natur, 558, 260